APPLIED SCIENCES AND ENGINEERING

Implantable wireless suture sensor for in situ tendon and ligament strain monitoring

Guangmin Yang[1,2], Rongzan Lin[3], Haojie Li[3], Yuqiu Chen[3], Meiling Liu[3], Ziyang Luo[3], Kewei Wang[3], Jinying Tu[3], Yue Xu[3], Zixiao Fan[3], Yizhi Zhou[3], Yongwei Pan[1,2], Zhe Zhao[1,2]*, Ran Liu[3]*

Tendon and ligament ruptures are prevalent, and severe sports injuries require surgical repair. In clinical practice, monitoring of tissue strain is critical to alert severe postoperative complications such as graft reinjury and loosening. Here, we present a sensor system that integrates a strain sensor and communication coil onto surgical silk sutures, enabling in situ monitoring and wireless readout of tissue strains via surgical implantation. The flexible sensor shows excellent adaptability to soft tissues, providing a strain monitoring range of 0 to 10% with a minimum detection threshold of 0.25% and maintaining stability more than 300,000 stretching cycles. The wireless sensor could be integrated with complex structures in surgical scenarios involving lateral collateral ligament injury and anterior cruciate ligament reconstruction, enabling distinct responses to graft stretching, reinjury, and loosening. Animal experiments demonstrate that the sensor can acquire real-time, clinical-grade strain data while exhibiting high biocompatibility. The sensor system shows considerable potential in evaluating preclinical implant performance and monitoring implant-related surgical complications.

INTRODUCTION

Tendons and ligaments are fibrous connective tissues that connect bone to muscle or bones, performing crucial functions such as load transmission, joint stability maintenance, and movement facilitation (*1*–*3*). In the United States, approximately 17 million ligament and tendon injuries require treatments each year, with more than 400,000 patients undergoing reconstructive surgery specifically for anterior cruciate ligament (ACL) tears (*3*–*5*). Human tendons and ligaments suffer irreversible damage when subjected to strains exceeding 8 to 10% (*4*, *6*). Post-rupture, inefficient tissue regeneration significantly diminishes the biomechanical properties due to poor blood supply and disorganized fibrosis (*5*, *7*). Surgical repair and graft implantation are commonly performed to restore the functionality of damaged tissue, aiming to re-establish normal anatomy and mechanical function. However, 3 to 25% of grafts fail following the initial surgery, and approximately 15% of patients experience reinjury post-discharge (*4*, *8*–*10*). Enhancing the outcomes of tendon and ligament surgery remains challenging due to the difficulty in acquiring the in vivo tissue strain status (*11*–*13*).

Integrating sensors with dense connective tissues such as ligaments or tendons is challenging due to its deep anatomical location, wide deformation range, and low tissue modulus. Therefore, designing a strain sensor for effective postoperative monitoring requires excellent anatomical conformity, minimal tissue irritation, high accuracy, and wireless communication capability. Current capacitive or resistive strain sensors show remarkable sensitivity, fatigue resistance, and continuous monitoring capabilities (*14*–*17*). However, several design issues should be addressed to meet clinical or preclinical application requirements. First, the sensor should securely attach to the target structure for accurate in situ monitoring. >>Flexible materials and adhesive hydrogels match the modulus of soft tissue. However, achieving secure adhesion remains a major challenge (*16*, *18*, *19*). Sensors assisted by additional attached connections or anchoring devices may also interfere with tissue function and damage flexible substrates (*11*, *20*). Second, degradable polyesters, polymers, metal particles, ionically conductive liquids, liquid metals, and carbon nanotubes are widely applied as sensing elements (*21*–*25*). In practice, these materials are susceptible to leakage and degradation in the ionic environment in vivo, potentially leading to sensor failure and potential toxicity risks (*26*, *27*). Furthermore, integrating passive, wireless devices and sensor signal collection systems presents a great challenge (*28*). Traditional power supply devices occupy considerable musculoskeletal space and require surgical removal, adding cost and adversely affecting patient rehabilitation (*11*, *23*, *26*).

In this study, we present a suture-based strain sensor functionalized with biocompatible conductive polymer poly(3,4-ethylenedioxythiophene)–poly(styrene sulfonate) (PEDOT:PSS) and encapsulated in medical-grade silicone. Medical sutures serve as the substrate for the sensor, facilitating tissue suturing and ensuring high biocompatibility. The functionalized sutures are woven into a double-helix configuration, creating a variable capacitance responsive to mechanical stretching (*29*). An inductance coil is integrated to enable wireless and real-time readout via an inductor and capacitor (LC) circuit. The suture-based sensor exhibited accurate monitoring capability and stability in 0 to 10% strain. Experiments conducted on porcine knee joints and rabbit Achilles tendons have demonstrated excellent monitor performance of the sensor within complex anatomical structures. The in vivo strain data provided by this sensor system also aids surgeons in monitoring implant-related complications; developing innovative, more kinematically accurate reconstruction techniques; and creating individualized rehabilitation programs.

RESULTS

Design and fabrication of the strain sensor

The longitudinally aligned filaments of surgical sutures produce irreversible elongation until break when overstretched (*30*). A double-helix structure allows the suture to undergo more stretching before

[1]School of Clinical Medicine, Tsinghua University, Beijing, China. [2]Center of Orthopaedics & Sport Medicine, Beijing Tsinghua Changgung Hospital, School of Clinical Medicine, Tsinghua University, Beijing, China. [3]School of Biomedical Engineering, Tsinghua University, Beijing 100084 China.
*Corresponding author. Email: zhaozhao_02@163.com (Z.Z.); liuran@tsinghua.edu.cn (R. Liu)

fully straightening. Furthermore, we encapsulated the sutures with elastic silicone, forming a composite structure of a fiber core and silicone elastomer outside. The double-helix composite sutures produce more strain when stretched, further expanding the strain range. We functionalized the sutures with conductive polymers to establish flexible capacitive strain sensor to achieve the electrical response to stretching. Based on the capacitive sensor, we constructed an inductance-capacitance circuit for wireless communication via inductive coupling. The system responds to strain by radiofrequency signals.

Figure 1A illustrates the application scenario of a strain sensor in ACL reconstruction. We integrated a wireless strain sensor with medical sutures so the system has the suturing function, enabling firm fixation to connective tissues and facilitating in vivo strain monitoring. The sensor system can be implanted intraoperatively to monitor soft tissue strain following tendon and ligament injury repair. The flexible strain sensor has two components with different elastic moduli: a nonresorbable surgical suture braided in a double helix and the spaced elastomer. The conductive sutures responsive to radiofrequency fields are functionalized with the conductive polymer PEDOT:PSS. Nonresorbable silk sutures (2-0) were selected as the sensor substrate due to compatibility with conductive polymers and extensive application in surgical procedures.

The functionalization and fabrication process of the sensor are depicted in Fig. 1B. PEDOT:PSS was selected over other conductive polymers for its superior stability on silk sutures. The degummed suture mainly comprises fibroin with an isoelectric point of about 4. Aqueous PEDOT:PSS dispersion featured with dissociated sulfonic acid and a pH of around 2 (*31*, *32*). The acidic dispersion ionizes the amino groups on the silk suture, causing the combination with the PEDOT:PSS and silk suture through strong electrostatic interactions, and has high stability after repeated ultrasonic cleaning (fig. S1) (*32*, *33*). The peeling-off tests with adhesive tape attached to conductive wires showed that while the PEDOT:PSS polymers could be peeled off, there was no significant increase in resistance increase in the multistranded threads compared with the single-stranded threads (figs. S2 and S3). This indicates that the functionalization creates a conductive network inside the multistranded suture that is barely affected by surface topography. The functional area of approximately 4 cm in the middle of the dewaxed sutures was soaked in PEDOT:PSS solution treated with dimethyl sulfoxide and ethylene glycol to obtain optimal conductivity (*34*–*36*). Through repeated soaking cycles, the sutures reached the desired level of conductivity (fig. S4). Conductive sutures were encapsulated by medical-grade silicone to form a capacitive dielectric layer with a specific thickness (figs. S5 and S6). Subsequently, the encapsulated sutures were twisted together, and liquid silicone was applied to the twisted sutures to solidify the double-helix configuration (movie S1). The double-helix configuration of the two coated sutures forms a variable capacitor that responds to strain. In an artificial physiological environment, the sensor exhibits stable capacitance for at least 8 weeks when placed in phosphate-buffered saline (PBS) (fig. S7). Figure 1C illustrates the suture sensor characterized by a plate spacing of 1200 μm, a pitch of 1.5 turns/cm, and a sensor length of 2 cm.

The scanning electron microscope (SEM) reveals the microstructure of the raw suture, the conductive polymer-treated suture, and the transverse view of the sensor (Fig. 2, A and C, and fig. S8). The SEM revealed that PEDOT:PSS was wrapped around the

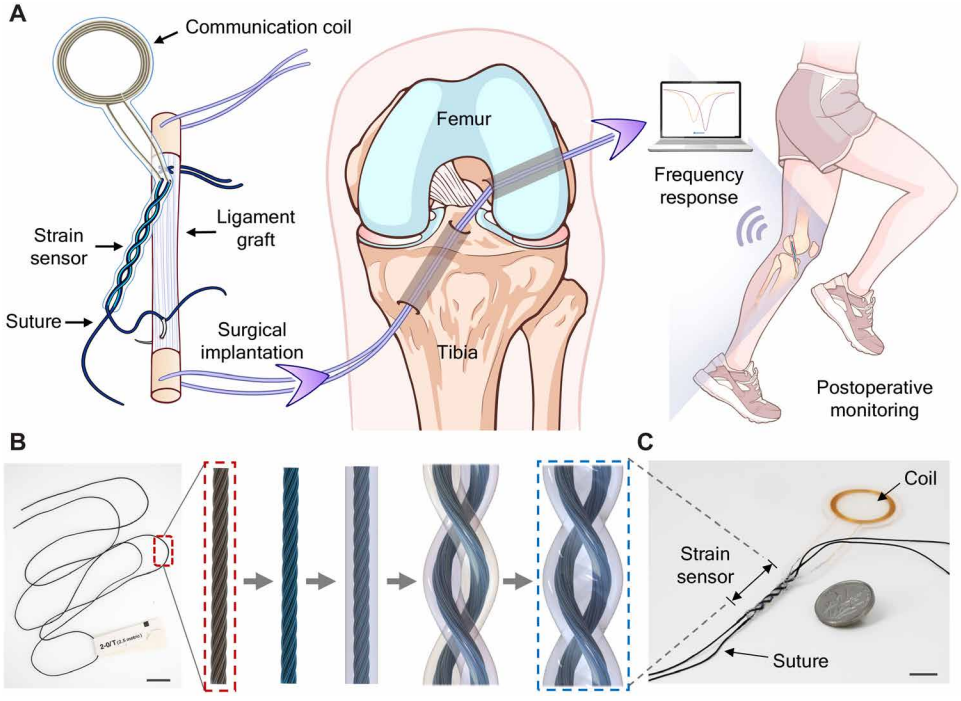

Fig. 1. Implantable wireless sensor for tendon and ligament strain monitoring through in situ suturing. (**A**) Schematic diagram of the implantation scenario of the strain sensing system. (**B**) Fabrication process of strain sensor from raw sutures, conductive sutures (functionalized with PEDOT:PSS), composite sutures (encapsulated with medical-grade silicon elastomer), and woven double helix capacitive sensor. Scale bar, 10 mm. (**C**) Photograph of the strain sensor system showing the sensor with a length of 2.0 cm, a pitch of 1.5 turns/cm, wire spacing of approximately 1200 μm, and a free wire length of 10 cm at both ends. Scale bar, 10 mm.

surface of the filaments inside the suture and filled between the filaments to form an interconnected conductive network (fig. S9). Furthermore, we encapsulated the sensor with a 2-μm coating of parylene-C in 5% prestretching to enhance waterproofing and suitability for in vivo implantation in a physiological pH environment (Fig. 2D and figs. S10 and S11).

As the double helix is stretched, the sutures straighten and move closer together, gradually reducing the distance between the sutures and generating strain in the sensor (Fig. 2, E and F, and movie S2). We established a structural simulation model to investigate the strain and capacitance pattern of the double-helix sensor. Finite element analysis (FEA) showed that the strain (0 to 10%) of the double-helix sensor during stretching was mainly concentrated in the elastomer packaging layer, and almost no strain was generated inside the sutures (Fig. 2G). Contrastingly, the non-twisted parallel sutures undergo a plastic strain of more than 1% strain, and the stretching after internal structural destruction would not produce a responsive capacitance (fig. S12A). Figure 2H illustrates that as the pitch of the double helix increases, the slope of the capacitance change curve gradually decreases while linearity improves. This indicates that increasing the double-helix pitches can extend the strain range but concurrently reduces sensitivity. Figure S13B further demonstrates that increasing the thickness of the spacing between the double-helix wires enhances the sensor linearity while also diminishing sensitivity. To explore the actual stretching behavior of the double-helix sensor, we prepared sensors with various encapsulation thicknesses and different pitches according to the simulation parameters. Figure S14A shows that a lower pitch (0.5 turns/cm) allows the sensor to straighten more quickly, resulting in higher sensitivity. However, this also narrows the linear range and limits the overall stretching range. Conversely, increasing the pitch (1.5 turns/cm) extends the linear range but reduces sensitivity. A thinner encapsulation layer allows the double helix to straighten more quickly and reach a $\Delta C/C_0$ of around 0.4, where C_0 is the initial capacitance and ΔC is the capacitance change. In contrast, a thicker encapsulation layer provides more linear behavior during stretching, although this comes at the cost of decreased sensitivity (fig. S14B). By planning the encapsulation thickness and pitch, the sensitivity and range

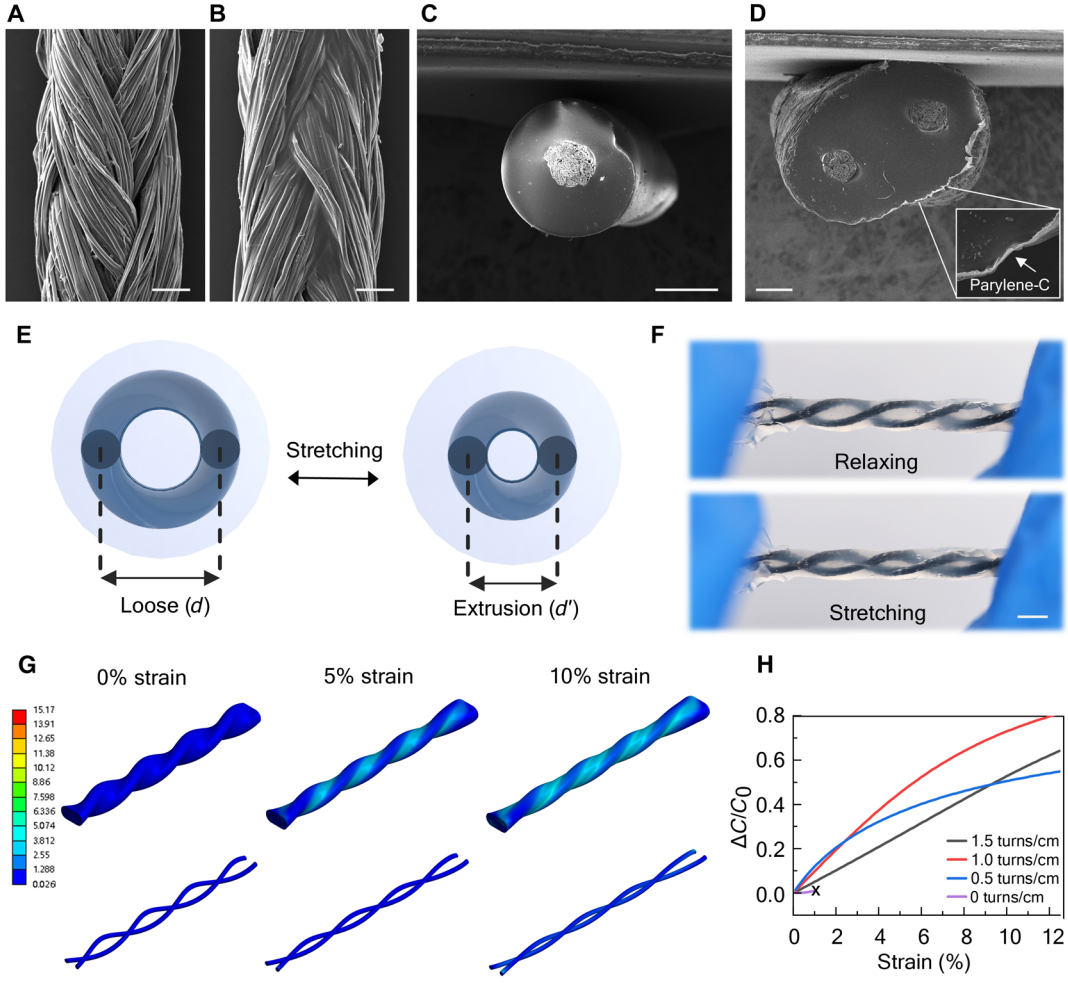

Fig. 2. Sensor functionalization and characterization. (**A** and **B**) SEM images of the multifilament silk sutures before and after PEDOT:PSS bonding. Scale bars, 100 μm. (**C**) Silk suture encapsulated with silicone elastomer. Scale bar, 500 μm. (**D**) SEM images depicting the transverse view of the sensor and a magnified view of parylene-C encapsulation. Scale bar, 500 μm. (**E**) Schematic illustration showing the spacing change in the transverse view of the sensor upon stretching, resulting in capacitance change. (**F**) Photographs of the suture sensor in relaxing and stretching conditions. Scale bar, 2 mm. (**G**) Strain behavior of the double-helix sensor in FEA. (sensor length, 2.0 cm; pitch, 1.5 turns/cm; and wire spacing, 1200 μm). (**H**) Equivalent capacitance changes in FEA with varying double-helix pitches from 0 to 10% strain.

of the sensor can be tuned to meet specific requirements. The strain tendons and ligaments generated during limb movement are commonly less than 10%. To minimize the space occupied by the sensor and cover the expected monitoring range, we prepared a strain sensor with a line spacing of 1200 μm and a pitch of 1.5 cm according to the sensor specifications used in the FEA and mechanical testing (*2, 11, 37, 38*).

Sensor performance

In the implantation scenario, the sensor preserves its origin length without requiring prestretching or additional tension, and its stress state is compatible with relaxed connective tissue. The monitoring range of the sensor begins at zero, allowing it to be implanted and secured along with the tendon or ligament in surgery, enabling full-scale and accurate monitoring. The tension-strain response of the sensor aligns with the natural stretching pattern of human tendons and ligaments; stress gradually increases as it approaches the tensile limit, resulting in a biomimetic *S*-shaped stress-strain curve until irreversible damage occurs to the sensor (Fig. 3A). When combined with ligament grafts, the suture sensor provides a potential mechanical advantage by improving the tensile strength of the tissue in addition to the monitoring capabilities (fig. S15).

The gauge factor of the sensor depends on the capacitance change that occurs during the stretching process of the double-helix sensor. For a strain range of approximately 10%, the capacitance change rate ($\Delta C/C_0$) of the suture sensor is about 0.5. The stretch curve of the double-helix sensor is close to linear during the stretching, making it suitable for monitoring tendon and ligament strain in actual movement (Fig. 3B). The repeatability of the strain sensor was verified by testing the sensor response of multiple double-helix sensors with identical parameters (fig. S16).

The strain sensor exhibits a typical hysteresis during the stretch-release cycle. Different elastic encapsulation materials may have an impact on the mechanical hysteresis of the sensor (Fig. 3C and fig. S17). Thus, tuning the viscoelasticity properties of the encapsulation material may mitigate sensor hysteresis. The elastic modulus of Ecoflex is about 0.1 MPa, which is closer to the elastic modulus of human subcutaneous soft tissue and muscle (0.01 to 0.1 MPa) (*39, 40*). With its excellent biocompatibility, Ecoflex was selected as the elastic substrate for implantable sensors to achieve better tissue conformity.

In the following testing, we used sensors with a pitch of 1.5 turns/cm and a wire spacing of 1200 μm. The sensor showed excellent stability and repeatability across various strain amplitudes (Fig. 3D). It maintained stability under both fast (up to 300 mm/min) and slow (1 mm/min) stretching speeds (Fig. 3E and fig. S18). Furthermore, the sensor exhibited high resolution in detecting minor strains within its designated range, providing stable and distinct responses to repeated tensile strains of 1, 0.5, and 0.25% (Fig. 3F and fig. S19).

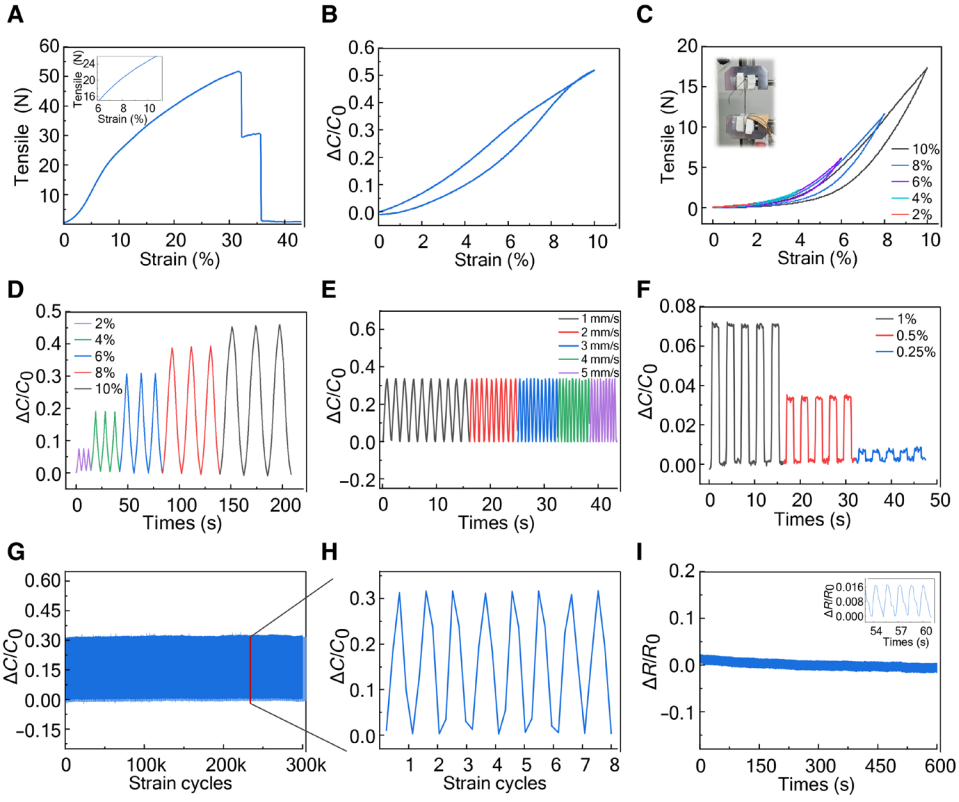

Fig. 3. Sensor performance. (**A**) Stress-strain curve of the suture sensor that closed to the characteristic curves of natural tendons and ligaments. A maximum tensile force of approximately 50 N on the sensor when subjected to more than 10% strain (sensor pitch, 1.5 turns/cm; wire spacing, 1200 μm). (**B**) Capacitance change rate of the sensor under the limiting strain of 10%. (**C**) Mechanical hysteresis of the suture sensor under 2 to 10% strain. (**D**) Stable and repeatable capacitive response under various applied strains (2, 4, 6, 8, and 10%). (**E**) Consistent sensor responses under stretch speeds ranging from 60 to 300 mm/min. (**F**) Minimum detectable strain of the sensor. (**G** and **H**) Fatigue cyclic curve and a detailed view of the sensor system more than 300,000 cycles when subjected to a strain equivalent to tear strain (~6%). (**I**) Resistance fluctuation of the conductive suture in cyclic stretching (~6% strain).

To explore reliability for in situ monitoring, we sutured the sensor onto ligament tissue and moistened the sensor and tissue with PBS to test the stability and durability of the sensor. When subjected to a strain value of 6%—representing the maximum elastic strain of ligaments and tendons—the sensor exhibited stable strain responses after more than 300,000 cycles without noticeable drift (Fig. 3, G and H). Further experiments revealed that the electrical resistance exhibited slight periodic changes (<1%) during cycles of straightening and rebounding, most likely attributed to the structural deformation of the suture filaments rather than permanent elongation (Fig. 3I). We conducted bending tests to evaluate the sensor performance during daily activities involving nonstretching posture movements. The test showed minimal interference in sensor signals in the nonstretching state, and the fluctuation values were lower than the minimum resolution threshold of the sensor (fig. S20).

Wireless circuit design

The strain sensor communicates wirelessly via a custom-designed radiofrequency system, as the circuit illustrated in Fig. 4A. The capacitive sensor (C) and a custom-designed inductive coil (L) are incorporated to form a passive LCR resonant circuit. The connection between the wire and the coil is secured by knotting, and the

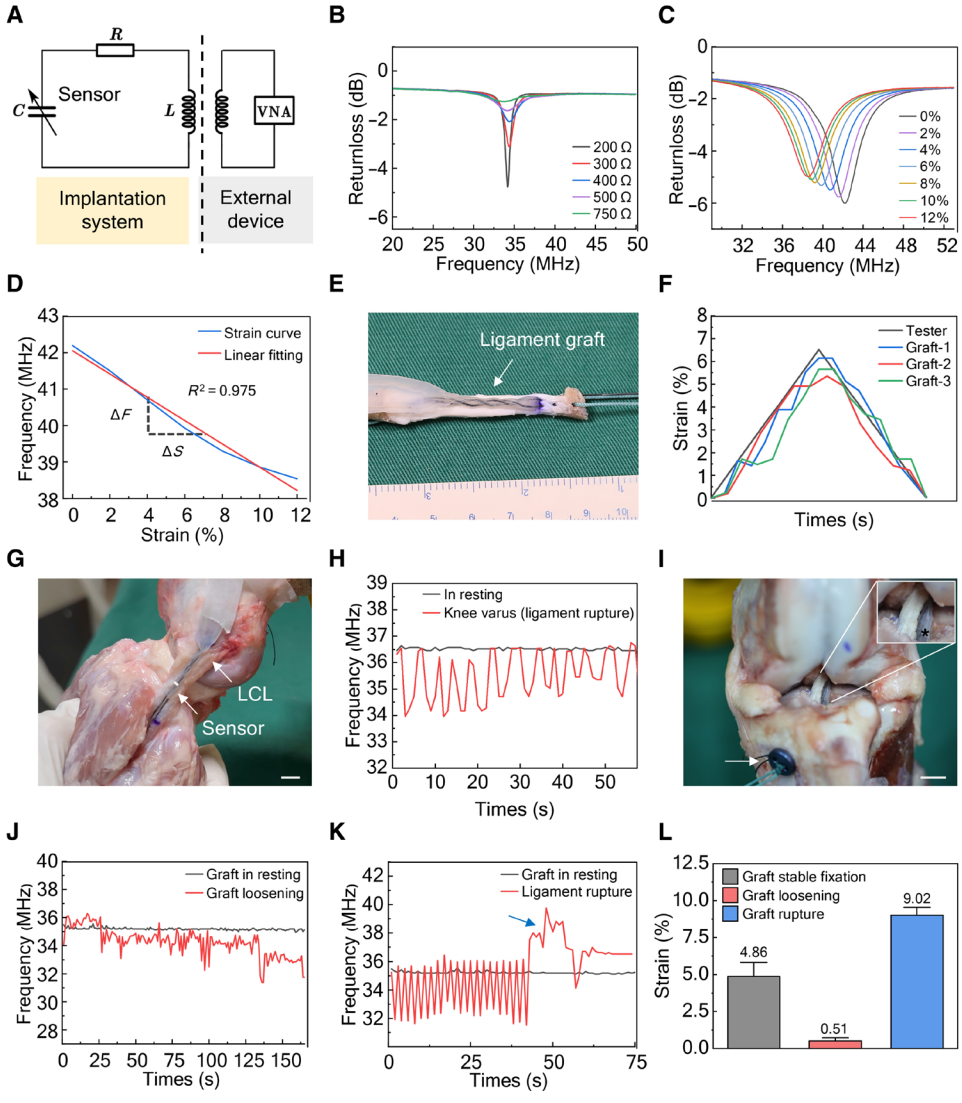

Fig. 4. In vitro implantation in porcine knee model. (**A**) Schematic diagram of the communication between implanted and external monitoring systems. VNA, Vector Network Analyzer. (**B**) Influence of various systematic resistances on the amplitude of the resonance peak. (**C**) The calibrated reflection coefficient (S_{11}) spectra of the sensor at various strains (0 to 12%). (**D**) Linear conversion of the coupling peak frequency of the sensor under different strains. (**E**) Sensor system and ligament graft complex after hand suturing. (**F**) Comparison of strain feedback between ligament in situ sensor and tensile testers under 6% strain. (**G**) Photograph of the lateral collateral ligament integrated with the sensor system. Scale bar, 10 mm. (**H**) Sensor responses on an injured lateral collateral ligament. (**I**) Photograph of the in situ graft-sensor complex after ACL reconstruction via tibia tunnel, with a magnified window showing the sensor and graft. Scale bar, 10 mm. (**J**) Disordered frequency response during the Lachman test in surgical-induced loosening experiments. (**K**) Increased frequency shifts, showing overstretching of the sensor in the surgical-induced injury to the ACL graft. The blue arrow denotes the point of complete rupture of the graft-sensor complex. (**L**) Statistics of sensor response under various conditions in the ACLR model ($P < 0.05$, $n = 5$). Gray, graft implanted solidly. Red, graft loosening. Blue, graft rupture. Error bars represent the SD.

surface is coated with PEDOT:PSS to enhance the circuit connection (fig. S21). The capacitance change produced by sensor stretching is monitored by the coupling of electromagnetic signals between the circuit and the external readout coil. When the suture sensor is affixed to the target tissue, changes in resonant frequency reveal the stretching of tendons or ligaments. The capacitive sensor converts structural elongation into shifts in the circuit resonant frequency. The resonant frequency of the LCR circuit can be calculated according to the following formula

$$f = \frac{1}{2\pi\sqrt{\mathrm{LC}}}$$

The scattering parameters (S_{11}) are detected by a portable vector network analyzer and presented on computer or mobile devices. A 12-turn single-layer titanium coil was used for wireless communication with an inductive range of 5 to 6 μH. Therefore, the expected resonance frequency range of the strain system is between 20 and 40 MHz. In this system, circuit resistance influences the amplitude of the resonant frequency (Fig. 4B). The system quality factor is about 0.5, which provides adequate resolution for minor strains. To obtain the precise response of the sensor to strain, each sensor underwent calibration before implantation (Fig. 4C). The frequency-strain curve is linearly transformed and fitted to obtain the formula characterized by intercept a and slope b (Fig. 4D)

$$f = a + b \cdot S$$

The strain output (ΔS) of the sensor during stretching can be calculated as follows

$$\Delta S = \Delta f / b$$

According to the strain formula, the ratio of the frequency change to the sensor slope (obtained by preimplantation calibration) quantifies the strain generated by the sensor. Typically, the coil is implanted subcutaneously, enabling patients to remove it surgically by an outpatient procedure after the period of high complication risk. Various tissue thicknesses and anatomical positions may affect coil coupling. We found that different coupling distances and offsets exhibit different frequency-strain curves, while the curve slopes were consistent (fig. S22). Therefore, the above formula can continue to be applied to calculate the strain. In addition, we could mark the location of the coil on the skin after implantation to improve the accuracy of coupling between coils. It has been demonstrated that materials with varying dielectric properties—such as air, ionic solution, and muscle tissue—do not significantly affect the coupling of the two coils (fig. S23). The circadian temperature rhythm of organisms fluctuates between 34.5° and 37.5°C, and the daily temperature variation ranges from 1° to 3°C (*41, 42*). To characterize the effect of temperature on sensor performance, we continuously tested the resistance and inductance of the sensor system when the ambient temperature was between 34° and 39°C. The maximum frequency drift of the sensor from 34° to 39°C is less than 0.25 MHz, and the corresponding strain is less than 1%, which will not affect sensor performance evidently. The resistance change value of the sensor is less than 1 ohm/cm, indicating that the system can maintain stable performance within the temperature range of the organism (fig. S24).

Wireless system implantation in cadaveric knee specimens

To investigate the potentiality of the wireless system in monitoring ligament strain, sensors were implanted in porcine knee joints. Because the strain sensor is designed based on surgical sutures, it can be implanted through a suture needle and secured with hand knots or suture buttons. Autologous grafts, commonly used in orthopedics surgery, were used to evaluate the performance of the sensor in detecting minor strains. Fresh bone-ligament-bone grafts were harvested from porcine knee joints, and sensors were sutured on both ends of the grafts using a suture needle. The sensor integration with the graft was performed intraoperatively on a graft prep board (fig. S25 and movie S3). Each sensor thread was sutured on the graft, starting from the insertion area and extending upward by four stitches (Fig. 4E). To explore the attachment and synchronous strain response of the sensors with the ligament, the sensor-graft composite was evaluated on a tensile tester, as depicted in fig. S26A. The results revealed a stable stress-strain curve in resting (fig. S26B) and synchronous response following sensor-tissue integration (Fig. 4F).

The cadaveric implantation process adheres to standard surgical protocols. Various fixation techniques were used to simulate typical injury scenarios and validate sensor reliability: trans-osseous button fixation for the lateral collateral ligament (LCL) and suture fixation on the bone-ligament-bone graft for ACL reconstruction (ACLR). The surgeon implanted the sensor without prestretching by manually adjusting the sutures, maintaining both the sensor and ligament at their original lengths, thereby more accurately reflecting in situ strain conditions. The LCL injury model was initially selected to evaluate the effectiveness of the sensor system on anatomical structures. Sensor wires were knotted using suture buttons on the medial cortex of the knee through trans-osseous bone tunnels at the LCL insertion points (Fig. 4G, and figs. S27 and S28). The function of LCL is to maintain the stability of the lateral side of the knee joint and produce strain when subjected to force to resist varus stress. Clinically, the knee varus test is used to diagnose LCL injuries, a positive test indicating LCL injury. Figure 4H and fig. S29 illustrate repetitive shifts in the resonant frequency, confirming that the LCL produces strain during the knee varus test. The signal-to-noise ratio (SNR) is defined as $\mathrm{SNR} = 10\log_{10}(f_2/f_0)$ dB, where f_2 and f_0 are the changes of the system center frequency under 2 and 0% strain, respectively. The sensor shows an SNR of 9.8 dB at 2% strain in the LCL implantation, with higher SNRs reachable under higher strain. When the ligament was artificially damaged and ruptured, evident changes in the resonant frequency of the sensor were observed during the knee varus (fig. S30 and movie S4), indicating overstretching of the tissue.

To explore the effectiveness of the sensor in complex structures and its performance in monitoring severe postoperative complications, we implanted it in the ACLR model (Fig. 4I). The widely accepted transtibial bone tunnel reconstruction technique was used, following standard surgical protocols, with detailed procedures outlined in the Supplementary Materials (figs. S31 and S32). The autograft carrying the sensor was secured to the cortex of the femur and tibia using suture buttons. In addition, the coil connected to the sensor was positioned under the skin of the medial tibia through the tibial tunnel to facilitate postoperative detection and removal. In the ACLR, assessing the tightness of the initial graft fixation poses a challenge in current clinical practice. Here, we addressed this challenge by evaluating initial graft fixation by detecting sensor frequency during graft testing, thereby providing data support for the initial fixation. Various scenarios of graft loosening, damage, and rupture were established through different surgical procedures, and the

strain monitored by the system was compared to validate the sensor performance (fig. S33).

Post-implantation, the sensor exhibited a stable frequency in the resting state. The Lachman test, a classic test for diagnosing ACL tears, was used to evaluate the sensor performance. When implanted in a healthy knee joint, the sensor exhibited stable, periodic signal changes by the Lachman test (fig. S34B). A positive Lachman test is indicative of forward laxity of the tibia and knee joint instability, which emphasizes the necessity for a solid graft to restore anterior-posterior stability in treatment. Following implantation, periodic resonant frequency shifts of the sensors were captured during Lachman testing of the ACLR model, indicating the restrictive effect of the sensor-graft combination on the knee joint (movie S5). Graft loosening and retearing are frequent causes of graft failure following ACLR. When performing the Lachmann test on a loose knee joint, we detected weakened and disorganized strain shifts, indicating inadequate graft function and predicting potential implant failure (Fig. 4J). In cases of graft reinjury, the sensor detects excessive stretching shifts in the target tissue, indicative of ligament elongation (fig. S34C). Figure 4K and fig. S34D illustrate the excessive strain following ACL graft rupture. Statistics of sensor response under various strain statuses in the ACLR model are shown in Fig. 4L.

Wireless system implantation in vivo

Before in vivo implantation, the sensor was cocultured with human skin fibroblasts (HSFs) in vitro to verify its biocompatibility. Biocompatibility was assessed by examining potential cytotoxicity, cell adhesion, metabolism, and proliferation. Green/red fluorescence images from the cell live/dead test demonstrated robust HSF proliferation on the sensor without significant apoptosis compared to the control group after several cell cycles (figs. S35 and S36). The Cell Imaging Kit and Cell Counting Kit-8 (CCK-8) test results indicated no significant difference in cell viability between the cocultured and control groups over multiple cell proliferation cycles, demonstrating excellent cell biocompatibility (fig. S37).

The sensor system was subjected to medical-grade high-temperature and autoclave sterilization (121.3°C, 103.4 kPa, ~30 min) before in vivo implantation (fig. S38). Considering the anatomical features of rabbits, we modified the sensor size to suit the length of the Achilles tendon and suturing the sensor onto the Achilles tendon using conventional methods (Fig. 5, A and B). The operation procedures are detailed in fig. S39. Surgically induced Achilles tendon injuries were applied in experiments to assess the efficacy of the sensor to monitor different strain states (Fig. 5C). The signal quality of the implanted system depends on the coupling between the coils. We place the attached coil subcutaneously to reduce the tissue barrier between the coils and place it on a flat area away from joints as much as possible to maintain the coupling between the coils during movement. For accurate signal acquisition, researchers may need to take more actions, such as drawing markers, adding magnetic cores, and applying slight body brakes to keep the coils aligned. After implantation, the transmitting coil attached to the thigh skin detects the receiving coil under the skin, generating a resonant spectrum (figs. S40 and S41). Figure 5D and fig. S40C illustrate changes in strain signals recorded on a computer in rabbit leg movements. The sensor exhibited specific frequency changes under rest and stretching and remained stable after different testing phases, demonstrating the possibility of long-term system use in vivo.

In the rabbit model of surgically induced Achilles tendon injury, evident resonant frequency shifts were observed during the squatting test 3 months post-implantation (Fig. 5E and movie S6). The resonant frequency in the Achilles tendon injury group was significantly greater than in the intact group, with an average strain of 9.42% (Fig. 5F). Portable ultrasound was used to monitor the stretching state of the sensor implanted in the Achilles tendon during follow-up (fig. S42 and movie S6). In the final experiment, tendon samples surrounding the sensor were harvested for histopathological analysis, revealing no excessive inflammatory reactions or tissue necrosis attributable to the implanted sensor (fig. S43). Masson staining and collagen volume fraction revealed that sensor suturing did not significantly affect the proportion or arrangement of collagen fibers in the tendon (Fig. 5, G and H). We further confirmed that implantation of the sensor system did not influence the fiber arrangement of the tendon by Sirius red staining (fig. S44).

The knee joint of sheep remains in an upright position, closely mimicking the kinematics of the human lower limbs. We implanted the sensor system into the patellar tendon of sheep to monitor tendon strain in movement (Fig. 5I and fig. S45). Following surgical implantation, as shown in fig. S45D, we attached the readout coil to the medial side of the tibia, corresponding to the position where the coil was embedded in the body. Under anesthesia, knee joint flexion was performed, and the periodic strain response of the sensor was obtained (fig. S46). After implantation, a wearable monitoring device was used to monitor the frequency response of the sensor during sheep movement (Fig. 5J). As shown in Fig. 5 (K and L), during movement, the sensor exhibited a corresponding strain response, thereby preliminarily showing the monitoring capability of the implanted device in living large animals.

DISCUSSION

In summary, this study developed a wireless, anatomy conformal strain sensor based on functionalized medical sutures for in situ monitoring of soft tissue strain in vivo. The double-helix sensor is tailored to match the strain characteristics of human tendons and ligaments, enabling precise monitoring of minor strains. The sensor design incorporates two crucial innovations with potential implications for future clinical translational study. First, the sensor is functionalized by medical-grade sutures, facilitating its integration into existing treatment modalities and reducing implantation difficulty. The streamlined sensor structure minimizes the impact of implanting extra devices on patient rehabilitation. The sensor integrates seamlessly with tissue, enduring the tension transmitted during human motion and accurately capturing deformations, superior to previously reported devices (*16*, *21*, *23*). Second, the sutures coated with elastomer are woven in a double-helix configuration combining soft- and high-modulus materials. The sensor initially stretches under stress, reflecting the flexibility typical of soft materials. Furthermore, it exhibits higher tensile resistance when almost fully straightened, preventing tissue overstretching. Our results demonstrate that the sensor can accurately measure strains while maintaining its tensile strength, providing insights for developing bionic artificial ligament materials with natural strain properties.

The injury mechanism of human tendons and ligament tissue in real sports scenarios is complex and changeable (*43, 44*). Traditional biomechanical experiments test isolated tissue in vitro under fixed

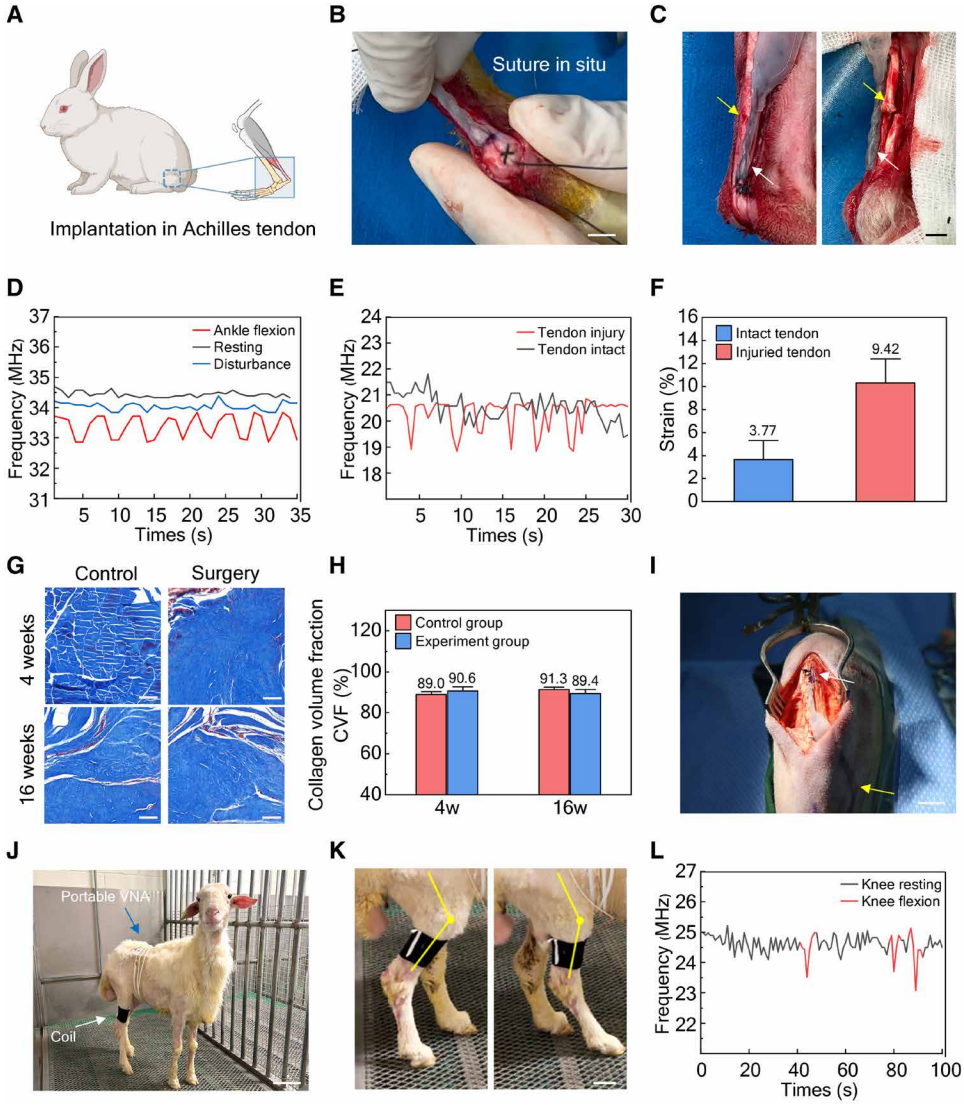

Fig. 5. Sensor implantation in vivo. (**A**) Schematic illustration of surgical implantation of the sensor in the Achilles tendon of New Zealand rabbits. (**B**) Image shows the sensor firmly fixed at the tendon end. Scale bar, 5 mm. (**C**) Sensor implantation in intact and half-severed Achilles tendon groups ($n = 6$, respectively). Scale bar, 5 mm. (**D**) Frequency patterns in various states in vivo: resting (red line), in limb swing (blue line), and repeated passive flexion and extension of the Achilles tendon (black line) (SNR = 3.6 dB). (**E**) Real-time sensor resonance frequency response during ankle joint flexion in the surgically induced Achilles tendon injury model, indicating tendon integrity damage and excessive tissue strain. (**F**) Statistics of sensor responses between healthy and tendon injury groups ($P < 0.05$, $n = 6$, respectively). (**G**) Transverse histopathologic images of tendon tissue at 4 and 16 weeks (Masson triple phase staining). Scale bars, 100 μm. (**H**) Quantitative analysis of collagen content in tendons with and without sensor implantation ($n = 6$, respectively). (**I**) Surgical image of sensor implantation in the sheep patellar tendon. Scale bar, 1 cm. (**J**) Photograph of experimental sheep with a wearable device and coil attached for strain monitoring. Scale bar, 10 cm. (**K**) Photograph of daily strain monitoring in sheep motion. Scale bar, 5 cm. (**L**) Strain response of the implanted sensor in knee flexion (SNR = 3.8 dB). Error bars represent the SD.

conditions, which makes it challenging to monitor the role of the target tendon or ligament in a dynamic musculoskeletal system. Therefore, the results obtained are only partially of reference significance to clinicians. The wireless strain system designed in this study can adapt in vivo strain monitoring under more complex conditions, and the results obtained are close to real scenarios. In this study, we preliminarily explored the strain conditions under different tissue states. However, most sensors fail to respond to strain effectively 3 months after implantation, mainly due to relaxation or destruction of the internal structure. About half (5 of 12) was due to sensor loosening caused by the migration of soft tissue in the fixed area, which showed that the implant system had good coupling with the reading coil, while no frequency changes in the joint flexion and extension. The remaining reasons included folding and breaking the communication coil (3 of 12), confirmed in the specimen harvest, which was manifested as no coupling frequency. Other reasons include sensor signal weakening and interference (4 of 12), which may be due to sensor destruction and water penetration of the sensor. The robustness of the implant system needs to be further improved to establish long-term, continuous monitoring solutions in complex application scenarios and motion states and to provide quantitative data support for the study of tissue injury mechanisms and postoperative sports strategies.

Future work to optimize the strain system can solve the following problems. First, the conversion from the coupling center frequency of the sensor on the vector network analyzer to the sensor data is done manually. Therefore, the quantitative analysis of the sensor data is not synchronized with the monitoring. Real-time data extraction and conversion algorithms can be developed to display exact strain information synchronously. Second, the degree of freedom of sensor monitoring is affected by the sensor design and is only along the long axis of the sensor. To obtain the strain data with more degrees of freedom, it may be necessary to implant more sensors or integrate sensors that monitor strain in different directions on one system to obtain more strain information on the tissue. We used silk sutures commonly used in clinical practice as the sensor substrate. Although silk sutures as the sensor substrate show good conformity with biological soft tissue, their insufficient strength affects further application as an additional reinforcement material and protective implant in surgery. Last, we used currently available nondegradable materials with high biocompatibility and stability to fabricate the system to maintain its performance after implantation. Biodegradable sensors avoid additional surgical removal and may bring more benefits to patients. Nevertheless, previous studies have reported that the performance of degradable sensors has continued to decline after implantation, which is the main factor affecting signal stability. Balancing the performance changes caused by the degradation process of strain sensors and the need for continuous monitoring are currently substantial obstacles that affect the transition of degradable sensors from laboratory to preclinical applications. The research on high-performance biodegradable materials and controllable packaging technology is promising for the future development of sensors (*14, 26, 45–47*).

MATERIALS AND METHODS

Conductive suture functionalization

The capacitive sensor was constructed using two 2-0 nonabsorbable braided sutures (Ethicon, Johnson & Johnson) and medical-grade silicone. Initially, the sutures underwent cleaning in a plasma cleaning machine for 5 min, followed by ultrasonic cleaning in N-methyl-2-pyrrolidone and absolute ethanol for 20 min to remove the wax film and impurities (*34*). The central 4 to 5 cm of the suture was soaked in 1.5% PEDOT:PSS solution (CLEVIOS PH1000, Heraeus) for 30 min to achieve conductive functionalization. During this soaking period, ultrasonic vibration was applied to expedite the process. The sutures were then removed and dried at 80°C. The functionalization step was repeated four times to increase the conductivity progressively.

Assembly of suture sensors

First, the conductive thread was wrapped with a layer of PDMS (SYLGARD 184, Dow) at a ratio of 7:1 PDMS to curing agent. The wires were positioned vertically to allow excess PDMS to drip off at room temperature, followed by drying in an oven at 80°C to achieve a smooth and insulated surface. Subsequently, the coated sutures were placed vertically, and Ecoflex 00-30 (Smooth-On.) was poured over them from top to bottom. Excess drops were removed from the bottom, and the wires were cured under a heating lamp at 100°C. This heating and curing process was repeated two to four times to achieve the desired coating thickness.

The assembly of the suture sensor was completed using a modified braiding machine with a coaxial motor. Each sensor consists of two insulated wires. One end of each wire was fixed to separate braiding machines, while the opposite ends were jointly fixed to a third machine. The braiding machine twisted one wire, while the opposite wounded the two strands together. This twisting action was designed to resist the pulling force caused by the axial deformation of the wire. The number of windings and the winding angle inside the sensor are adjustable using the braiding parameters. Last, Ecoflex was poured to secure the double helix configuration. The parylene-C layer was deposited onto the sensor surface by chemical vapor deposition using a parylene deposition instrument (SCS Labcoter 2). The powdered precursor is heated (165°C) and evaporated under vacuum to form a dimer gas. The gas is then pyrolyzed (690°C), and the dimer is decomposed into monomers, which polymerize on the sensor surface at room temperature (25°C) with the gas flow. The vacuum deposition process lasts about 6 hours to form a transparent polymer film with a thickness of 2 μm. The sensor model and schematic diagram presented in this article were created using SolidWorks (v2021, Dassault).

Sensor characteristics and strain simulation

The microstructure of the sensor was examined using an environmental electron microscope (Quanta 200). The capacitor response to stress and strain was evaluated using a multifunctional tensile tester (ZHIQU), with each test conducted on a minimum of three samples. Sensor geometry was modeled using SolidWorks, while the stretching behaviors were stimulated using Ansys (v2021). The material behavior of the suture and Ecoflex was performed using the isotropic elastic model (diameter: 0.4 mm, Young's modulus: 200 MPa, Poisson's ratio: 0.23, density: 3000 kg/m^3, tensile yield strength: 220 MPa) and the YEOH hyperplastic model (C10: 17000, C20: 200, C30: 23; D1: 20, D2: 15, D3: 10; density: 1270 kg/m^3), respectively. The finite element model was meshed using tetrahedrons (element size: 0.10 mm). More details can be found in previous studies (*48*). The simulation process excluded dynamic deformation of the internal structure of the braided wire.

Assembly of the wireless sensor system

The wireless passive LCR system comprises the sensor and a connected inductive coil. The coil was constructed from 0.15-mm-diameter titanium (Ti) wire, coated with medical-grade polyurethane for insulation. The silver wire was wound into a planar inductive coil with 12 turns and was approximately 2 cm in diameter. Junctions between the coil wiring and wire strain sensor were securely bonded, and an insulation coating was applied following PEDOT:PSS immersion. The in vitro signal detection circuit comprises a portable network analyzer and computer analysis software (WiMo).

In vitro model validation

Knee joint specimens were obtained from 1-year-old pigs ($n = 5$) sourced from the food industry, exempt from animal ethics considerations. In the LCL repair model, the LCL was cleaned before suturing the sensor wire near its fibular and femoral insertions. This facilitated the passage of sensor threads through these tunnels, which were then secured with button sutures at both ends. In the ACL reconstruction model, the ACL was dissected, and either the medial or lateral ligament was used to create a bone-tendon-bone graft implantation. Bone tunnels were established at the tibial plateau and lateral femoral condyle using comprehensive techniques to facilitate ligament and sensor fixation. The implants were secured using suture buttons.

Cell viability

HSFs were cultured with the sensor in 24-well plates to study its effect on cell viability. Before culturing, the sensor was sterilized using high temperature and high pressure (121°C, 0.1 MPa) and thoroughly washed with PBS to remove impurities. Cell suspension (2×10^4 to 5×10^4 per well) and culture medium were sequentially added to the well plate and placed in an incubator (37°C, 5% CO_2, ~40% humidity). To explore the cytotoxicity of the sensor and its impact on cell proliferation, the Live/Dead Cell Imaging Kit and CCK-8 from Servicebio were used. The Live/Dead Cell Imaging principle relies on two probes that detect intracellular esterase activity and cell membrane integrity, reflecting cell viability and cytotoxicity: Calcein AM stains live cells, producing green fluorescence (E_x/E_m, 488/515 nm), while propidium iodide stains dead cells, emitting red nuclear fluorescence (E_x/E_m, 570/602 nm). Quantitative cell proliferation and cytotoxicity analysis were performed using the CCK-8 kit, which measures mitochondrial dehydrogenase activity. The reduction of WST-8 dye produces an orange-yellow formazan compound with absorbance at 450 nm, directly correlating with the number of viable cells and indicating higher absorbance with increased cell proliferation. Live/Dead Cell Imaging was analyzed using a 10× laser confocal microscope and its accompanying software, while a microplate reader was used for the CCK-8 quantitative analysis.

Animal experiments and histocompatibility

The ethics committee of Tsinghua University approved the animal protocols for this study (23-LR1). Twelve female New Zealand rabbits, with an average weight of 3 kg, were included in the study. All procedures were conducted at the Tsinghua University Animal Experiment Center with personnel qualified for animal surgeries. Anesthesia was administered using Zoletil 50 at 0.8 to 1.2 ml/kg (Virbac). The lower limbs of the rabbits were disinfected and draped following standard protocols. A posterior incision was made to expose the Achilles tendon where the sensor was sutured at the distal insertion, and the proximal end was sutured at the junction of the Achilles tendon and muscle. The coil was placed subcutaneously on the lateral aspect of the femur to align with the external detection device. The incision was cleaned with saline and diluted iodophor before wound closure. Postoperative care included daily administration of painkillers and antibiotics for 3 days. The rabbits regained the ability to walk 1-day post-operation, facilitating signal detection.

In the sheep study, a 2-year-old female sheep weighing approximately 62 kg ($n = 1$, with bilateral implantation) underwent surgical disinfection and draping. The knee joint was marked with a sterile marker, and a 5- to 8-cm incision was made from the patella to the insertion point of the tibial tubercle. The patellar tendon was exposed by separating the tissue layer. The suture positions for the sensor on the patellar tendon were marked: the distal position at the upper edge of the tibial tubercle and the proximal position at the patella-tendon junction. Suturing of the sensor commenced at the proximal end. During distal suturing, the knee joint was maintained near full extension to relax the tendon, and the sensor tension was adjusted to ensure it was not stretched relative to the patellar tendon before securing it with a knot. Vascular forceps were used to free the subcutaneous connective tissue around the knee joint, and the sensor coil was positioned on the anteromedial aspect of the tibia for postoperative detection. Postoperative wound closure and perioperative management followed the same procedures described for the New Zealand rabbit experiment.

Supplementary Materials

The PDF file includes:
Figs. S1 to S46
Legends for movies S1 to S6

Other Supplementary Material for this manuscript includes the following:
Movies S1 to S6

REFERENCES AND NOTES

1. G. Yang, B. B. Rothrauff, R. S. Tuan, Tendon and ligament regeneration and repair: Clinical relevance and developmental paradigm. *Birth Defects Res. C Embryo Today* **99**, 203–222 (2013).
2. L. Bobzin, R. R. Roberts, H. J. Chen, J. G. Crump, A. E. Merrill, Development and maintenance of tendons and ligaments. *Development* **148**, dev186916 (2021).
3. D. L. Butler, N. Juncosa, M. R. Dressler, Functional efficacy of tendon repair processes. *Annu. Rev. Biomed. Eng.* **6**, 303–329 (2004).
4. J. A. Luque-Seron, I. Medina-Porqueres, Anterior cruciate ligament strain in vivo: A systematic review. *Sports Health* **8**, 451–455 (2016).
5. N. L. Leong, J. L. Kator, T. L. Clemens, A. James, M. Enamoto-Iwamoto, J. Jiang, Tendon and ligament healing and current approaches to tendon and ligament regeneration. *J. Orthop. Res.* **38**, 7–12 (2020).
6. P. Sharma, N. Maffulli, Tendon injury and tendinopathy: Healing and repair. *J. Bone Joint Surg. Am.* **87**, 187–202 (2005).
7. W. L. Lim, L. L. Liau, M. H. Ng, S. R. Chowdhury, J. X. Law, Current progress in tendon and ligament tissue engineering. *Tissue Eng. Regen. Med.* **16**, 549–571 (2019).
8. A. M. Seitz, L. Dürselen, Biomechanical considerations are crucial for the success of tendon and meniscus allograft integration-a systematic review. *Knee Surg. Sports Traumatol. Arthrosc.* **27**, 1708–1716 (2019).
9. B. Sonnery-Cottet, A. Saithna, M. Cavalier, C. Kajetanek, E. F. Temponi, M. Daggett, C. P. Helito, M. Thaunat, Anterolateral Ligament reconstruction is associated with significantly reduced acl graft rupture rates at a minimum follow-up of 2 years: A prospective comparative study of 502 patients from the SANTI Study Group. *Am. J. Sports Med.* **45**, 1547–1557 (2017).
10. S. J. Meredith, T. Diermeier, B. B. Rothrauff, V. Musahl, F. H. Fu, "6 - Anterior cruciate ligament" in *Evidence-Based Management of Complex Knee Injuries*, R. F. LaPrade, J. Chahla, Eds. (Elsevier, 2022), pp. 77–89.
11. Q. Zhang, N. C. Adam, S. H. H. Nasab, W. R. Taylor, C. R. Smith, Techniques for in vivo measurement of ligament and tendon strain: A review. *Ann. Biomed. Eng.* **49**, 7–28 (2021).
12. M. J. Bey, K. A. Derwin, Measurement of in vivo tendon function. *J. Shoulder Elbow Surg.* **21**, 149–157 (2012).
13. F. H. Fu, K. Nagai, Editorial commentary: The anterior cruciate ligament is a dynamic structure. *Arthroscopy* **34**, 2476–2477 (2018).
14. Y. Luo, M. R. Abidian, J. H. Ahn, D. Akinwande, A. M. Andrews, M. Antonietti, Z. Bao, M. Berggren, C. A. Berkey, C. J. Bettinger, J. Chen, P. Chen, W. Cheng, X. Cheng, S. J. Choi, A. Chortos, C. Dagdeviren, R. H. Dauskardt, C. A. Di, M. D. Dickey, X. Duan, A. Facchetti, Z. Fan, Y. Fang, J. Feng, X. Feng, H. Gao, W. Gao, X. Gong, C. F. Guo, X. Guo, M. C. Hartel, Z. He, J. S. Ho, Y. Hu, Q. Huang, Y. Huang, F. Huo, M. M. Hussain, A. Javey, U. Jeong, C. Jiang, X. Jiang, J. Kang, D. Karnaushenko, A. Khademhosseini, D. H. Kim, I. D. Kim, D. Kireev, L. Kong, C. Lee, N. E. Lee, P. S. Lee, T. W. Lee, F. Li, J. Li, C. Liang, C. T. Lim, Y. Lin, D. J. Lipomi, J. Liu, K. Liu, N. Liu, R. Liu, Y. Liu, Y. Liu, Z. Liu, Z. Liu, X. J. Loh, N. Lu, Z. Lv, S. Magdassi, G. G. Malliaras, N. Matsuhisa, A. Nathan, S. Niu, J. Pan, C. Pang, Q. Pei, H. Peng, D. Qi, H. Ren, J. A. Rogers, A. Rowe, O. G. Schmidt, T. Sekitani, D. G. Seo, G. Shen, X. Sheng, Q. Shi, T. Someya, Y. Song, E. Stavrinidou, M. Su, X. Sun, K. Takei, X. M. Tao, B. C. K. Tee, A. V. Thean, T. Q. Trung, C. Wan, H. Wang, J. Wang, M. Wang, S. Wang, T. Wang, Z. L. Wang, P. S. Weiss, H. Wen, S. Xu, T. Xu, H. Yan, X. Yan, H. Yang, L. Yang, S. Yang, L. Yin, C. Yu, G. Yu, J. Yu, S. H. Yu, X. Yu, E. Zamburg, H. Zhang, X. Zhang, X. Zhang, X. Zhang, Y. Zhang, Y. Zhang, S. Zhao, X. Zhao, Y. Zheng, Y. Q. Zheng, Z. Zheng, T. Zhou, B. Zhu, M. Zhu, R. Zhu, Y. Zhu, Y. Zhu, G. Zou, X. Chen, Technology roadmap for flexible sensors. *ACS Nano* **17**, 5211–5295 (2023).
15. J. Yi, G. Zou, J. Huang, X. Ren, Q. Tian, Q. Yu, P. Wang, Y. Yuan, W. Tang, C. Wang, L. Liang, Z. Cao, Y. Li, M. Yu, Y. Jiang, F. Zhang, X. Yang, W. Li, X. Wang, Y. Luo, X. J. Loh, G. Li, B. Hu, Z. Liu, H. Gao, X. Chen, Water-responsive supercontractile polymer films for bioelectronic interfaces. *Nature* **624**, 295–302 (2023).
16. C. M. Boutry, Y. Kaizawa, B. C. Schroeder, A. Chortos, A. Legrand, Z. Wang, J. Chang, P. Fox, Z. Bao, A stretchable and biodegradable strain and pressure sensor for orthopaedic application. *Nat. Electron.* **1**, 314–321 (2018).
17. X. Hu, J. Huang, Y. Wei, H. Zhao, S. Lin, C. Hu, Z. Wang, Z. Zhao, X. Zang, Laser direct-write sensors on carbon-fiber-reinforced poly-ether-ether-ketone for smart orthopedic implants. *Adv. Sci.* **9**, e2105499 (2022).
18. B. R. Freedman, A. Kuttler, N. Beckmann, S. Nam, D. Kent, M. Schuleit, F. Ramazani, N. Accart, A. Rock, J. Li, M. Kurz, A. Fisch, T. Ullrich, M. W. Hast, Y. Tinguely, E. Weber,

D. J. Mooney, Enhanced tendon healing by a tough hydrogel with an adhesive side and high drug-loading capacity. *Nat. Biomed. Eng.* **6**, 1167–1179 (2022).
19. D. Wirthl, R. Pichler, M. Drack, G. Kettlguber, R. Moser, R. Gerstmayr, F. Hartmann, E. Bradt, R. Kaltseis, C. M. Siket, S. E. Schausberger, S. Hild, S. Bauer, M. Kaltenbrunner, Instant tough bonding of hydrogels for soft machines and electronics. *Sci. Adv.* **3**, e1700053 (2017).
20. S. S. Karipott, B. D. Nelson, R. E. Guldberg, K. G. Ong, Clinical potential of implantable wireless sensors for orthopedic treatments. *Expert Rev. Med. Devices* **15**, 255–264 (2018).
21. J. Lee, S. J. Ihle, G. S. Pellegrino, H. Kim, J. Yea, C.-Y. Jeon, H.-C. Son, C. Jin, D. Eberli, F. Schmid, B. L. Zambrano, A. F. Renz, C. Forró, H. Choi, K.-I. Jang, R. Küng, J. Vörös, Stretchable and suturable fibre sensors for wireless monitoring of connective tissue strain. *Nat. Electron.* **4**, 291–301 (2021).
22. A. Frutiger, J. T. Muth, D. M. Vogt, Y. Mengüç, A. Campo, A. D. Valentine, C. J. Walsh, J. A. Lewis, Capacitive soft strain sensors via multicore-shell fiber printing. *Adv. Mater.* **27**, 2440–2446 (2015).
23. F. Sheng, B. Zhang, Y. Zhang, Y. Li, R. Cheng, C. Wei, C. Ning, K. Dong, Z. L. Wang, Ultrastretchable organogel/silicone fiber-helical sensors for self-powered implantable ligament strain monitoring. *ACS Nano* **16**, 10958–10967 (2022).
24. T. Li, Y. Li, T. Zhang, Materials, structures, and functions for flexible and stretchable biomimetic sensors. *Acc. Chem. Res.* **52**, 288–296 (2019).
25. G. Yao, L. Kang, C. Li, S. Chen, Q. Wang, J. Yang, Y. Long, J. Li, K. Zhao, W. Xu, W. Cai, Y. Lin, X. Wang, A self-powered implantable and bioresorbable electrostimulation device for biofeedback bone fracture healing. *Proc. Natl. Acad. Sci. U.S.A.* **118**, e2100772118 (2021).
26. L. Cai, A. Burton, D. A. Gonzales, K. A. Kasper, A. Azami, R. Peralta, M. Johnson, J. A. Bakall, E. Barron Villalobos, E. C. Ross, J. A. Szivek, D. S. Margolis, P. Gutruf, Osseosurface electronics-thin, wireless, battery-free and multimodal musculoskeletal biointerfaces. *Nat. Commun.* **12**, 6707 (2021).
27. O. A. Araromi, M. A. Graule, K. L. Dorsey, S. Castellanos, J. R. Foster, W. H. Hsu, A. E. Passy, J. J. Vlassak, J. C. Weaver, C. J. Walsh, R. J. Wood, Ultra-sensitive and resilient compliant strain gauges for soft machines. *Nature* **587**, 219–224 (2020).
28. J. Park, B. Seo, Y. Jeong, I. Park, A review of recent advancements in sensor-integrated medical tools. *Adv. Sci.* **11**, e2307427 (2024).
29. H. H. Shi, Y. Pan, L. Xu, X. Feng, W. Wang, P. Potluri, L. Hu, T. Hasan, Y. Y. S. Huang, Sustainable electronic textiles towards scalable commercialization. *Nat. Mater.* **22**, 1294–1303 (2023).
30. S. E. Naleway, W. Lear, J. J. Kruzic, C. B. Maughan, Mechanical properties of suture materials in general and cutaneous surgery. *J. Biomed. Mater Res. B Appl. Biomater.* **103**, 735–742 (2015).
31. A. Lund, S. Darabi, S. Hultmark, J. D. Ryan, B. Andersson, A. Ström, C. Müller, Roll-to-roll dyed conducting silk yarns: A versatile material for E-textile devices. *Adv. Mater. Technol.* **3**, 1800251 (2018).
32. J. D. Ryan, D. A. Mengistie, R. Gabrielsson, A. Lund, C. Müller, Machine-washable PEDOT:PSS dyed silk yarns for electronic textiles. *ACS Appl. Mater. Interfaces* **9**, 9045–9050 (2017).
33. S. Darabi, M. Hummel, S. Rantasalo, M. Rissanen, I. Öberg Månsson, H. Hilke, B. Hwang, M. Skrifvars, M. M. Hamedi, H. Sixta, A. Lund, C. Müller, Green conducting cellulose yarns for machine-sewn electronic textiles. *ACS Appl. Mater. Interfaces* **12**, 56403–56412 (2020).
34. V. Kalidasan, X. Yang, Z. Xiong, R. R. Li, H. Yao, H. Godaba, S. Obuobi, P. Singh, X. Guan, X. Tian, S. A. Kurt, Z. Li, D. Mukherjee, R. Rajarethinam, C. S. Chong, J. W. Wang, P. L. R. Ee, W. Loke, B. C. K. Tee, J. Ouyang, C. J. Charles, J. S. Ho, Wirelessly operated bioelectronic sutures for the monitoring of deep surgical wounds. *Nat. Biomed. Eng.* **5**, 1217–1227 (2021).
35. X. Fan, W. Nie, H. Tsai, N. Wang, H. Huang, Y. Cheng, R. Wen, L. Ma, F. Yan, Y. Xia, PEDOT:PSS for flexible and stretchable electronics: Modifications, strategies, and applications. *Adv. Sci.* **6**, 1900813 (2019).
36. C. Sun, X. Li, J. Zhao, Z. Cai, F. Ge, A freestanding polypyrrole hybrid electrode supported by conducting silk fabric coated with PEDOT:PSS and MWCNTs for high-performance supercapacitor. *Electrochim. Acta* **317**, 42–51 (2019).
37. J. D. Hassebrock, M. T. Gulbrandsen, W. L. Asprey, J. L. Makovicka, A. Chhabra, Knee ligament anatomy and biomechanics. *Sports Med. Arthrosc. Rev.* **28**, 80–86 (2020).
38. B. C. Fleming, B. D. Beynnon, P. A. Renstrom, R. J. Johnson, C. E. Nichols, G. D. Peura, B. S. Uh, The strain behavior of the anterior cruciate ligament during stair climbing: An in vivo study. *Arthroscopy* **15**, 185–191 (1999).
39. D. J. Sut, P. Sethuramalingam, Design optimisation and an experimental assessment of soft actuator for robotic grasping. *Int. J. Intell. Robot. Appl.* **8**, 758–786 (2024).
40. C. F. Guimarães, L. Gasperini, A. P. Marques, R. L. Reis, The stiffness of living tissues and its implications for tissue engineering. *Nat. Rev. Mater.* **5**, 351–370 (2020).
41. J. Waterhouse, B. Drust, D. Weinert, B. Edwards, W. Gregson, G. Atkinson, S. Kao, S. Aizawa, T. Reilly, The circadian rhythm of core temperature: Origin and some implications for exercise performance. *Chronobiol. Int.* **22**, 207–225 (2005).
42. T. Miyake, Y. Inoue, Y. Maekawa, M. Doi, "Circadian clock and body temperature" in *Thermal Biology: Temperature Sensing and Temperature-Responding Systems*, M. Tominaga, M. Takagi, Eds. (Springer Nature, 2024), pp. 177–188.
43. M. Gilgien, J. Spörri, J. Kröll, P. Crivelli, E. Müller, Mechanics of turning and jumping and skier speed are associated with injury risk in men's World Cup alpine skiing: A comparison between the competition disciplines. *Br. J. Sports Med.* **48**, 742–747 (2014).
44. N. A. Mall, P. N. Chalmers, M. Moric, M. J. Tanaka, B. J. Cole, B. R. Bach Jr., G. A. Paletta Jr., Incidence and trends of anterior cruciate ligament reconstruction in the United States. *Am. J. Sports Med.* **42**, 2363–2370 (2014).
45. W. Heng, S. Yin, J. Min, C. Wang, H. Han, E. Shirzaei Sani, J. Li, Y. Song, H. B. Rossiter, W. Gao, A smart mask for exhaled breath condensate harvesting and analysis. *Science* **385**, 954–961 (2024).
46. C. Xu, Y. Song, J. R. Sempionatto, S. A. Solomon, Y. Yu, H. Y. Y. Nyein, R. Y. Tay, J. Li, W. Heng, J. Min, A. Lao, T. K. Hsiai, J. A. Sumner, W. Gao, A physicochemical-sensing electronic skin for stress response monitoring. *Nat. Electron* **7**, 168–179 (2024).
47. E. Shirzaei Sani, C. Xu, C. Wang, Y. Song, J. Min, J. Tu, S. A. Solomon, J. Li, J. L. Banks, D. G. Armstrong, W. Gao, A stretchable wireless wearable bioelectronic system for multiplexed monitoring and combination treatment of infected chronic wounds. *Sci. Adv.* **9**, eadf7388 (2023).
48. D. Steck, J. Qu, S. B. Kordmahale, D. Tscharnuter, A. H. Muliana, J. Kameoka, Mechanical responses of Ecoflex silicone rubber: Compressible and incompressible behaviors. *J. Appl. Polym. Sci.* **136**, 47025 (2019).

Acknowledgments

Funding: This work was supported by the National Key R&D Program of China (grant 2023YFC3502700 to R.L.), the Beijing Municipal Natural Science Foundation (grant nos. L223035 to R.L. and L232089 to Z.Z.), the Tsinghua University Initiative Scientific Research Program of Precision Medicine (grant 2022PY001 to R.L.), the National Natural Science Foundation of China (grant nos. 82072093, 82027807, and U22A20355 to R.L.), and the Tsinghua University–Xiamen Chang Gung Hospital Joint Research Center for Anaphylactic Disease (grant no. 20202910218 to R.L.). **Author contributions:** Conceptualization: G.Y., Z.Z., and R. Liu. Methodology: G.Y., R. Lin, Z.Z., and H.L. Investigation: G.Y., R. Lin, H.L., Y.C., M.L., and K.W. Visualization: G.Y., R. Lin, Y.Z., J.T., Y.X., Z.L., and Z.F. Supervision: Y.P., R. Lin, Z.Z., and R. Liu. Writing—original draft: G.Y. and Z.Z. Writing—review and editing: G.Y., R. Lin, Z.Z., R. Liu, and J.T. **Competing interests:** The authors declare that they have no competing interests. **Data and materials availability:** All data needed to evaluate the conclusions in the paper are present in the paper and/or the Supplementary Materials.

Submitted 25 September 2024
Accepted 28 January 2025
Published 28 February 2025
10.1126/sciadv.adt3811